Ostwald ripening in a two-dimensional system: Correlation effects

Oleg Krichevsky and Joel Stavans
Department of Physics of Complex Systems, Weizmann Institute of Science, Rehovot 76100, Israel
(Received 3 January 1995)

We report results from an experimental study of coarsening in thin layers of succinonitrile in the presence of impurities. By quenching the latter from the liquid phase to different temperatures within the liquid-solid coexistence region, different solid area fractions ϕ are obtained. As ϕ is incresed from 0.13 to 0.40, liquidlike order develops among the coarsening crystals due to diffusional interactions. The latter give rise to local correlations between the size and rate of growth of crystals within a neighborhood of size $\xi(\phi)$. We study these and compare our findings with recent theoretical models of coarsening.

PACS number(s): 64.60.Qb, 64.70.Dv, 05.70.Fh

I. INTRODUCTION

When a homogeneous binary mixture is quenched to sufficiently low temperatures it separates into two phases, each characterized by a different concentration of the two constituents [1]. The phase separation process starts in off-critical mixtures by the nucleation of droplets of the minority phase, which grow in size and number within the majority phase. The volume fraction ϕ occupied by droplets grows in time until the volume of both phases nearly attains the equilibrium values as specified by the lever rule. Finally, in the late stages of the separation process, no more droplets form and the existing ones undergo a coarsening process whereby big droplets grow at the expense of small ones that shrink and disappear. This coarsening process, known as Ostwald ripening [2], is driven by the tendency of the system to minimize its total surface energy, and is mediated by the diffusion of the constituents. A mean-field theoretic description of Ostwald ripening in three-dimensional systems was first proposed by Lifshitz and Slyozov [3] and by Wagner [4] (LSW), who assumed that the diffusion field around each droplet is given by a solution to the diffusion equation for an isolated spherical particle. This assumption is valid only when the droplets of the minority phase are very far away from each other, i.e., in a nearly zero volume fraction situation, in which case a droplet's rate of growth is determined solely by its radius, and the degree of supersaturation of the majority phase. These two parameters define a critical radius above which droplets grow and below which droplets shrink. This assumption enabled LSW to solve their model in an analytic and closed form, and to obtain two predictions that can be readily tested in an experiment. First, the average droplet radius $\bar{R}$ grows with time t as a power law Kt^{α}, with $\alpha=\frac{1}{3}$ and the rate constant K having a constant value depending solely on the diffusion constant, the surface tension, and the degree of supersaturation. Second, the distribution of droplet sizes $f(R,t)$ reaches a material-independent universal form when properly scaled. LSW calculated this universal distribution within the framework of their model. The value of α, which can be obtained by simple and very general dimensional arguments, has been amply confirmed in numerous experiments [5–11] and numerical studies [12–17]. However, these studies have also revealed that K is much larger than expected, and that the scaled size distribution is broader and more symmetric than the shape predicted by the LSW model, even at volume fractions of the order of a few percent. Worse, the observed deviations increase with the volume fraction ϕ. Experiments have also shown that at high enough values of ϕ, the shape of the droplets is not spherical as assumed by LSW and that the droplets may migrate as a result of their interaction through their diffusion fields [18].

The origin of the discrepancies between the experimental observations and the LSW model lies in its basic assumption. At finite values of ϕ, the diffusion field around a droplet assumed by LSW is perturbed by the presence of other droplets [19]. The mutual influence of the diffusion fields around two nearby droplets promotes the accelerated shrinkage of one and growth of the other, the rates of shrinkage and growth being larger than if both droplets were isolated. Thus shrinking droplets are more likely to be found in the neighborhood of growing ones and vice versa. The rate constant is therefore increased, and the rates of evolution of nearby droplets are correlated *(medium polarization effect)* [20]. Furthermore, small droplets are more likely to be found near large ones *(direct correlation effect)* [21,22]. These two effects are responsible for broadening the droplet size distribution. These correlations complicate considerably any theoretical description, since many-body effects have to be incorporated. The problem has been tackled by various statistical mechanical theories and numerical simulations that introduce finite-ϕ effects perturbatively (the appropriate small parameter in the perturbation expansion being $\sqrt{\phi}$ as first recognized by Tokuyama and Kawasaki [21]), or that assume that shrinking or growing droplets act as pointlike sources or sinks (monopole approximation to the diffusion field). The perturbative calculations are quite complicated, and therefore have been carried out only to first order in $\sqrt{\phi}$, a fact that limits the validity of these investigations to small values of ϕ. Fortunately, both the direct correlation effect and the medium polar-

ization effect appear already to first order in $\sqrt{\phi}$ in the perturbative calculations, and the behavior of the droplet size distribution observed in experiments is reproduced qualitatively. Notably, few experimental investigations of Ostwald ripening in three-dimensional systems have provided direct evidence for correlations, beyond the broadening of the size distribution function [18].

The main obstacle that has prevented the straightforward generalization of these ideas to two-dimensional systems is the logarithmic divergence of the solution of the two-dimensional diffusion equation for $\phi \rightarrow 0$, where ϕ now denotes the droplet area fraction. The effects of this divergence have been circumvented by Rogers and Desai [23] who have performed an asymptotic analysis appropriate for this limit, and found a generalization of the LSW size distribution function, and that $\bar{R} \sim (t/\ln t)^{1/3}$. In their approach, the only length scale in the problem is the droplet radius. Models for $\phi \neq 0$ (the relevant length scales are now determined by ϕ itself and $\bar{R}$) have been put forward by various authors [17,24–29]. The picture that emerges from these models is essentially the same as for three-dimensional systems: the growth law $\bar{R} \sim t^{1/3}$ is not affected by correlation effects (a result that is supported by computer simulations [17,30]), and the size distribution function is increasingly broadened with ϕ (in some of the models [17,26] the distribution function reduces to the form obtained by Rogers and Desai in the limit $\phi \rightarrow 0$). As in three dimensions, these approaches fail for $\phi \sim 0.1$ and above. Surprisingly, the problem of Ostwald ripening in two-dimensional systems has not been an object of much experimental scrutiny. Studies of coarsening in diblock copolymer films have not provided data in the scaling regime, nor tackled the issue of correlations [31]. Patterns of coarsening domains in amphiphilic monolayers at the air-water interface exhibit dynamical scaling, but a growth exponent below the LSW, presumably due to the prominent role of electrostatic interactions among domains [32]. Other studies have addressed nonrelated issues [33].

In this paper we present the results of an experimental study of Ostwald ripening in two dimensions for area fractions ϕ in the range $0.13 < \phi < 1$, focusing our attention on correlation effects. Our system consists of thin layers of succinonitrile, quenched into the liquid-solid coexistence region. A brief account of our findings has already been published [34]. Our main goal has been to exhibit correlation effects explicitly so that the results will provide a benchmark against which the predictions of the different theoretical models can be tested. A decisive advantage of our experiments over those on three-dimensional systems is that correlations can be measured directly. In three dimensions they have to be inferred either from stereological analysis of two dimensional cuts, or from measurements of scattered radiation. The latter depend on both the structure factor (which contains information on correlations) and the form factor of a set of droplets of unknown polydispersity and shape. In addition, we can follow the evolution of the system in real time, with all the details of the evolution being accessible. The price we pay, however, is that we cannot reach very small values of ϕ without a considerable loss in the statistical accuracy of our measurements.

Our paper is organized as follows: in the next section, we skim over key features of existing theoretical models, and introduce some concepts we will make use of in analyzing our experimental data. In Sec. III we provide details about our experimental setup and finally in Sec. IV we present our results.

II. THEORETICAL BACKGROUND

The essential ideas behind correlated growth are captured best by drawing a formal analogy between Ostwald ripening and electrostatics. We follow Marder's arguments, originally formulated for three-dimensional systems [22]. The starting point of his statistical mechanical model, which builds upon ideas of Weins and Cahn [19], and Kawasaki and Ohta [35], is a static diffusion equation with shrinking and growing droplets of spherical shape, appearing as sink and source terms:

$$\nabla^2 c(r,t) = \sum_{i=1}^{N} \frac{d}{dt}\left[\frac{4\pi}{3} R_i^3\right] \delta(r - r_i) \ . \tag{1}$$

In writing this equation, a quasistationary approximation has been assumed according to which the concentration is everywhere relaxed to its local equilibrium value. The concentration at the surface of the ith droplet is determined via the Gibbs-Thomson relation $c(r,t) = d_0/R_i$, where d_0 is a capillary length. The analogy with electrostatics is evident: our problem is formally equivalent to solving for the electrostatic potential around conducting spheres of radii R_i, the potential on which is d_0/R_i respectively. Equation (1) is a Poisson equation in which the rate of change of the volume of each droplet plays the role of a charge. Thus shrinking droplets have a negative charge while those that grow are associated with a positive charge. Marder showed that in the limit in which the average droplet size is much smaller than the distance over which diffusion has acted (this is true except right after the formation of a droplet), one can obtain an average solution of the form:

$$c(r) = \frac{e^{-r/\xi}}{r} \ .$$

Thus the diffusion field away from a droplet has the form of screened Coulomb potential in which the screening length ξ is given by

$$\xi = \left[\frac{1}{4\pi n \bar{R}}\right]^{1/2} ,$$

where n is the droplet number density. Notice that since the volume fraction occupied by the droplets is given by $\phi = (4\pi R^3 n/3)$, ξ can be expressed as $\xi/R = (3\phi)^{-1/2}$ so that ξ diverges in the limit of vanishing ϕ. Marder carried out a perturbative expansion to first order in $\sqrt{\phi}$, and was able to show by intuitive arguments that the rate of growth of a droplet including the (averaged) presence of all the other droplets includes the direct and medium polarization effects.

The singular behavior of the solution of the two-

dimensional diffusion equation precludes the use of the strategy adopted for the three-dimensional problem, namely, solving the $\phi=0$ problem first, and then including correlations later. Rogers and Desai handled this singular behavior by performing an asymptotic analysis of the diffusion equation. As a result, they obtained a growth law of the form $\bar{R}\sim(t/\ln 4t)^{1/3}$ and the following scaling form for the size distribution function, which is a generalization of the LSW distribution to two dimensions:

$$f(x)=\begin{cases} Cx^2\left[1-\frac{2x}{3}\right]^{-28/9}\left[1+\frac{x}{3}\right]^{-17/9}\exp\left[\frac{-2/3}{1-2x/3}\right] & \text{for } x<1.5\ , \\ 0 \quad \text{for } x\geq 1.5\ . \end{cases} \tag{2}$$

Here $x=R/\bar{R}$ and C is a normalization constant. This distribution will be henceforth called the LSW distribution. Different schemes have been devised to circumvent the singular behavior of the diffusion equation in the finite-ϕ case. Chakraverty [24] introduced a screening distance to cut off the Coulomb interaction between three-dimensional droplets on a substrate, while Dadyburjor, Marsh, and Glicksman [25] and Hayakawa and Family [26] established screening by calculating analytically the diffusion field of a droplet array. Ardell's theory of coarsening circular clusters included the effect of diffusional interactions through the introduction of an *ad hoc* cutoff distance [27]. At this distance the boundary condition fixing the concentration field to have the bulk value is satisfied. The size distribution predicted by his model was expectedly broader than the LSW distribution proposed by Rogers and Desai [Eq. (2)], but agreed reasonably well with their computer simulation. In addition, it reduced to Eq. (2) in the limit $\phi\rightarrow 0$. Marqusee [28] included the medium polarization effect in his model by considering surrounding droplets as an effective medium. He added a term $-\xi^{-2}c(r,t)$ to the right-hand side of Eq. (1) turning it into a Helmholtz equation, and thereby removing the logarithmic divergence of the diffusion equation. He solved his model self-consistently and obtained $\bar{R}\sim t^{1/3}$, the prefactor $K(\phi)$, the screening length $\xi(\phi)$ for different values of ϕ, and the increasing broadening of the scaled size distribution for increasing ϕ. Zheng and Gunton [29] extended Marqusee's theory to include the direct correlation effect. They showed that its effect is smaller than medium polarization but that the scaled size distribution is significantly changed (mainly for small radii), and that the power-law growth $t^{1/3}$ remains unaffected. The authors expected their scheme to be valid for $\phi<0.01$. Yao *et al.* [17] included both direct and medium polarization correlations in their recent model. They approximated correlation effects in a way analogous to the Thomas-Fermi approach in Coulomb systems and obtained power-law growth $t^{1/3}$, and the asymptotic scaled size distribution. The latter in particular reduces to the LSW distribution for $\phi\rightarrow 0$. However, these calculations break down for $\phi>0.085$.

In our experiments we access a regime of area fraction where many of the assumptions made in the studies described above are questionable. However, in the absence of a proper theoretical framework to treat this case, we still find the electrostatic analogy to be helpful in discussing our results.

III. EXPERIMENTAL SETUP AND MATERIALS

Our experiments were carried out by quenching a thin layer of succinonitrile, a plastic crystal of bcc structure, from the high-temperature homogeneous liquid phase, to the liquid-solid coexistence region, which opens up in the presence of impurities. Succinonitrile presents the following advantages: it is a nearly transparent compound, the surface tension of the liquid-solid interface has very small anisotropy ($\approx 0.5\%$), and its melting temperature is slightly above room temperature. We used 99% pure succinonitrile purchased from Fluka. The impurities (1%) can be regarded as the second constituent of a binary mixture. Their presence opens up a liquid-solid coexistence region (43–56 °C) shown schematically in Fig. 1, in which the solid area fraction can be controlled by varying the temperature, as in temperature-composition phase diagrams of binary mixtures. Two processes are involved in the evolution of the system: heat and impurity diffusion. By making the latter dominant, we ensure

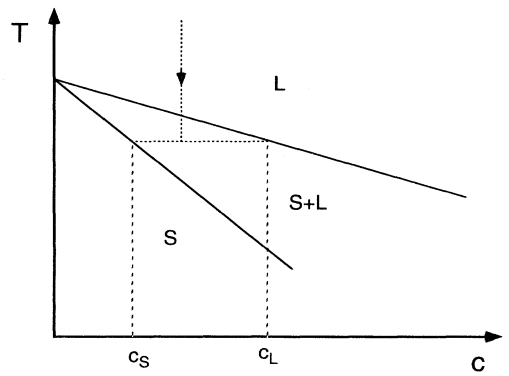

FIG. 1. Concentration-poor portion of the schematic temperature T vs impurity concentration c phase diagram of our system. Solidus and liquidus lines (solid lines) divide the plane into solid (S), liquid (L), and solid-liquid (S-L) coexistence regions. Samples are quenched from L into the S-L region (dashed lines), reaching eventually equilibrium with the solid (liquid) phase having an impurity concentration $c_s(c_l)$.

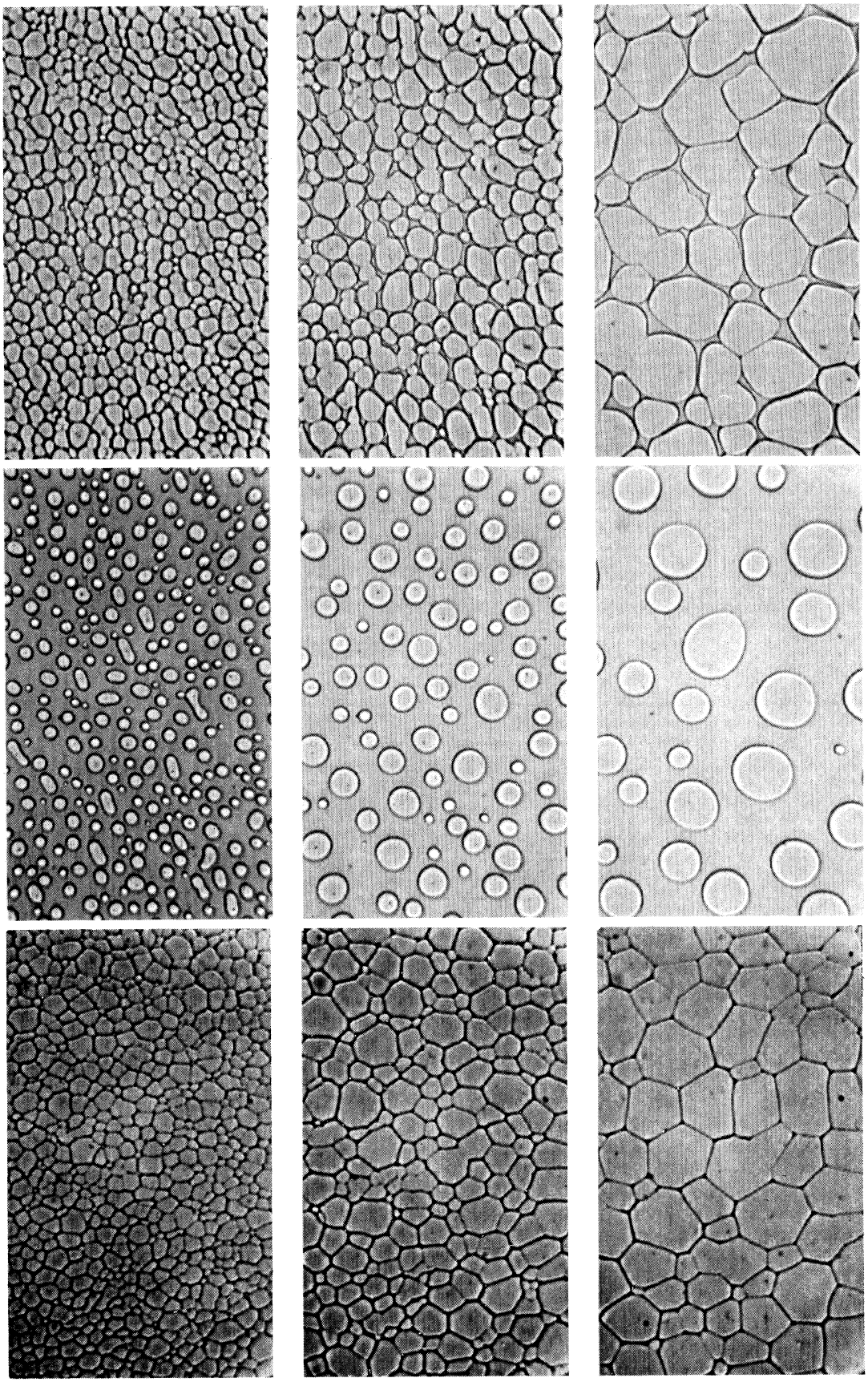

FIG. 2. Snapshots of part of the system coarsening at three different values of the temperature T. Left: cellular structure evolution ($\phi=1$) at $T=38\,^{\circ}\mathrm{C}$ (snapshot times from top to bottom: 15, 110, and 540 min); center: coarsening at $T=54\,^{\circ}\mathrm{C}$ where crystals are well separated, filling a fraction $\phi=0.3$ of the total area (times: 16, 145, and 1440 min); right: partial melting along grain boundaries at $T=43\,^{\circ}\mathrm{C}$ (times: 20, 120, and 1440 min). The images are about 2.5 mm across.

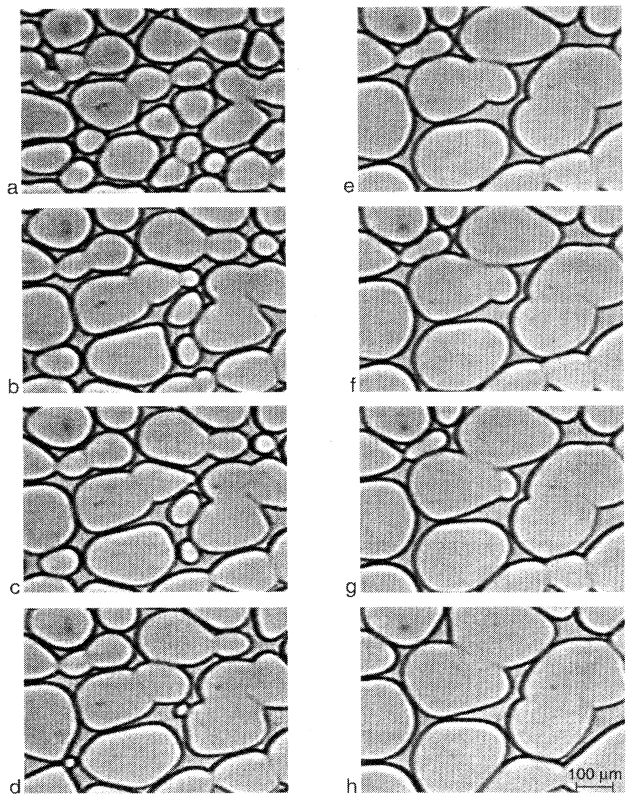

FIG. 3. Evolution of a region in our system at $T=43\,^{\circ}\mathrm{C}$. Snapshot times: (a) 104, (b) 260, (c) 291, (d) 342, (e) 505, (f) 536, (g) 563, and (h) 679 min. Focusing on the central part of each snapshot, notice the presence of two evolution processes: the Ostwald ripening mechanism (a) and (b), and recrystallization events such as creation (c)–(f), and disappearance (g) and (h) of grain boundaries. The area fraction is 0.9 in this case.

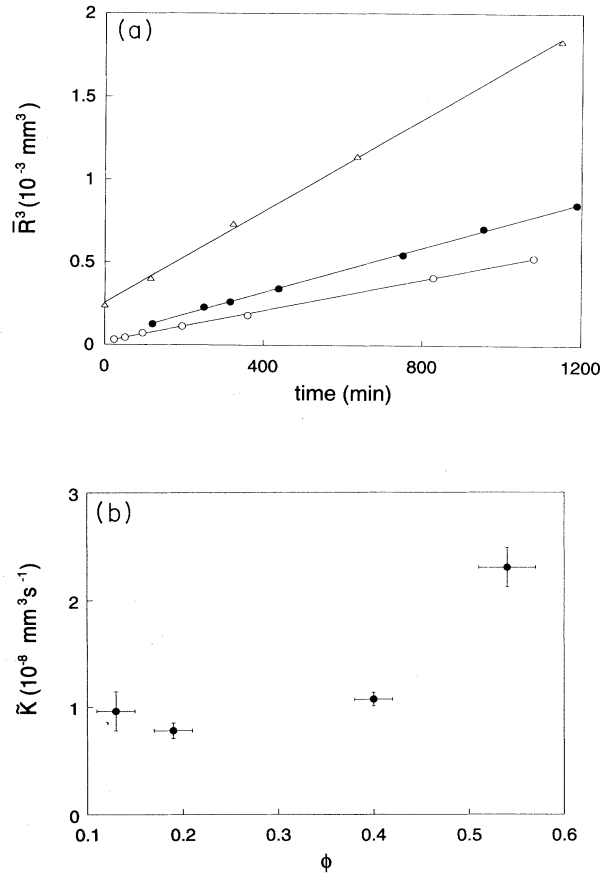

FIG. 4. (a) Power-law dependence of the average crystal radius $\bar{R}$ as a function of time for $\phi=0.19$ (empty circles), 0.40 (full circles), and 0.54. Straight lines are fits to the data with the equation $\bar{R}^3+R_0^3=\tilde{K}t$. (b) Dependence of the rate constant $\tilde{K}$ on volume fraction ϕ.

in-plane diffusion, as heat can leak out of the system through the walls of our cells. The experiments were carried out in 25-μm-thick samples contained in cells made out of glass slides. The thermal conductivity of succinonitrile is 0.224 W/mK, which is very similar to that of the glass slides used to manufacture our cells. However, experiments carried out in cells made out of sapphire, whose conductivity is more than ten times that of succinonitrile yielded essentially the same results as those performed in glass-made cells, confirming that impurity diffusion is the dominant process in our system. The pressure in the cells was maintained constant at atmospheric value. Before each run, samples were annealed for 24 h in an oven in order to avoid large impurity gradients. In order to create many crystal seeds initially, our samples were quenched to nearly 0 °C after which the temperature was raised to desired values within the liquid-solid coexistence region. Typically about 1000 crystallites were observed in the field of view after a quench. Their shape was at this point contorted and elongated, due to the fast

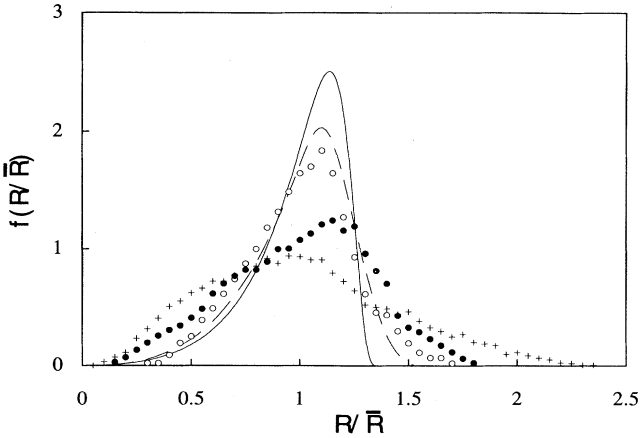

FIG. 5. Distribution of grain size $f(R)$ for $\phi=0.13$ (empty circles), 0.40 (full circles), and 1.00 (crosses). The solid line is the LSW generalized to the two-dimensional case by Rogers and Desai. The dashed line represents the theoretical results of Levitan and Domany for $\phi=0.13$.

growth induced by the deep quench. In order to avoid any influence of initial conditions and due to limits in resolution, our measurements were taken when the number of crystals ranged from 300 to 30. Thus nearly a decade in the number of crystals was spanned during each run. The lateral dimensions of the crystals were much larger than the layer thickness, ensuring the effective two dimensionality of our system. During the coarsening process, the temperature of the samples was maintained constant with a precision of ± 10 mK. The area fraction of the solid phase was constant within 3% along each run. Patterns were observed by optical microscopy, video recorded, and digitized for further analysis.

IV. RESULTS

In Fig. 2 we show snapshots taken at different times during three runs, each at a different temperature T. At $T=38\,^{\circ}\mathrm{C}$ (left), the plane is fully tiled ($\phi=1$) by solid crystallites of nearly polygonal shape and random crystallographic orientation. Grain boundaries have been made visible by adding a small amount of rhodamine dye to the sample before the quench. Notice (i) the occasional occurrence of very weakly stained boundaries and (ii) the marked deviation from120° in the angles between each of these boundaries and the two others meeting at a vertex. This is a manifestation of the fact that different boundaries have different line tensions. Despite this, the evolution in this case proceeds very much along the same lines as that of other cellular structures such as coarsening two-dimensional froths [36]: grains with less than six sides shrink and disappear according to von Neumann's theorem [37], while their neighbors grow. When a grain disappears, it alters the number of sides of some of its neighbors and a dynamical steady state with scaling properties is established: statistical distributions, when properly rescaled, preserve their shape under the evolution. A detailed study of this regime of evolution, known as *recrystallization*, has appeared recently [38]. At high temperatures, well-separated crystals within a liquid matrix are observed. The evolution then proceeds via the Ostwald ripening mechanism. This is shown in the central snapshots of Fig. 2 (taken at $T=54\,^{\circ}\mathrm{C}$), where crystals fill up a fraction $\phi\sim 0.30$ of the total area. Deviations from circular shape are clearly evident in the present case (the more elongated shapes observed in the earliest pattern are due to initial conditions; the evolution quickly relaxes these shapes into the characteristic noncircular morphologies of the scaling regime shown in the second and third snapshots). Note, however, that these deviations become smaller as the area fraction is decreased. At intermediate temperatures, the system is in the solid-liquid coexistence region, and partial melting along the grain boundaries is observed. An example of the evolution in this case is shown in the right part of Fig. 2. In these snapshots, taken at $T=43\,^{\circ}\mathrm{C}$, crystals occupy a fraction of 0.9 of the total area. Notice the contorted and occasional nonconvex shape of the grains. In this regime the shape is determined by both the surface tension of the solid-liquid interface and the particular line

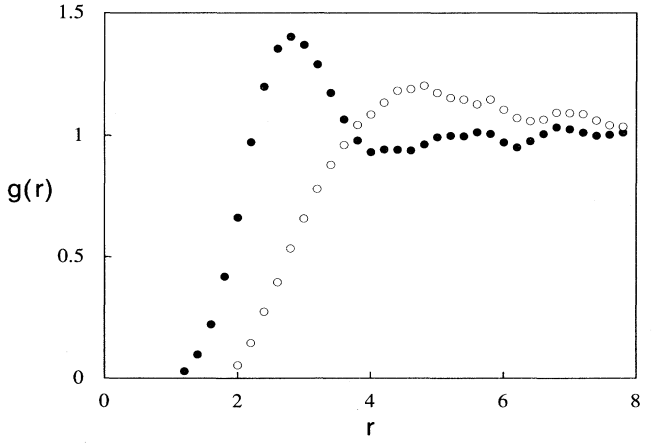

FIG. 6. Radial pair distribution function $g(r)$ for two different values of the area fraction ϕ, 0.13 (empty circles) and 0.40 (full circles), showing the evolution of gaslike behavior for low ϕ to liquidlike behavior at higher values of ϕ. Distances are given in units of the average radius $\bar{R}$.

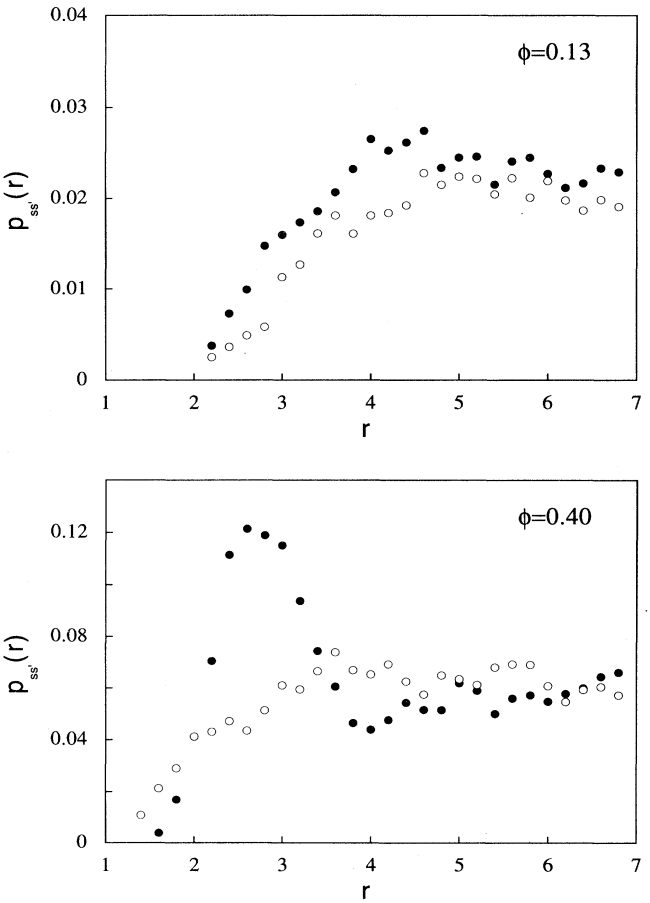

FIG. 7. Probability densities of finding two crystals both with radii smaller or larger than $\bar{R}$ at a distance r (empty circles) and of one having radius smaller and the other larger than $\bar{R}$ (full circles), for $\phi=0.13$ and 0.40. Distances are given in units of $\bar{R}$.

tension of the grain boundaries. The evolution is then governed simultaneously by recrystallization processes as well as by the Ostwald ripening mechanism (see the sequence of snapshots in Fig. 3). Note that recrystallization is only relevant for very large values of ϕ, when different crystals touch one another as a result of shape relaxation, and thus form grain boundaries.

In Fig. 4(a) we plot the cube of the average radius $\bar{R}$ as a function of time for three different values of the volume fraction ϕ: 0.19, 0.40, and 0.54. The average is taken over all crystals in a pattern. The data fall to a very good approximation on straight lines, and have been fitted with linear relations $\bar{R}^3+R_0^3=\tilde{K}t$. This confirms once again the celebrated power-law dependence t^α with $\alpha=\frac{1}{3}$. We also extracted from our data the dependence of the rate constant $\tilde{K}$ on ϕ, which we show in Fig. 4(b). While $\tilde{K}$ increases with ϕ as expected, it is very difficult to compare the behavior with theoretical predictions [28] since we vary ϕ by changing the temperature of our system, and doing so changes the microscopic kinetics of the system as well. Nonetheless, the relative increase in $\tilde{K}$ we observe in the volume fraction range 0.10–0.40 is consistent with theoretical predictions (these reach $\phi=0.40$ only).

The measured size distribution functions $f(R)$ with R given in units of $\bar{R}$ are shown in Fig. 5, for $\phi=0.13$, 0.40, and 1.0 (53, 49, and 38 °C, respectively), together with the LSW distribution Eq. (2). For a given value of ϕ, the shape of $f(R)$ does not change with time within our statistical accuracy, a fact that allows us to average measurements of distributions obtained at different times during the scaling regime. Each distribution shown in Fig. 5 is an average over ten such measurements. The distribution for $\phi=0.13$ is compared with recent theoretical results for this volume fraction [39]. In the last two cases, the radii refer to those of circles having the same area as each crystal in a pattern. Each distribution comprises measurements on ten patterns recorded in the scaling regime. As ϕ increases the distributions become flatter and broader, in agreement with the behavior predicted by theoretical models and computer simulations. Note that

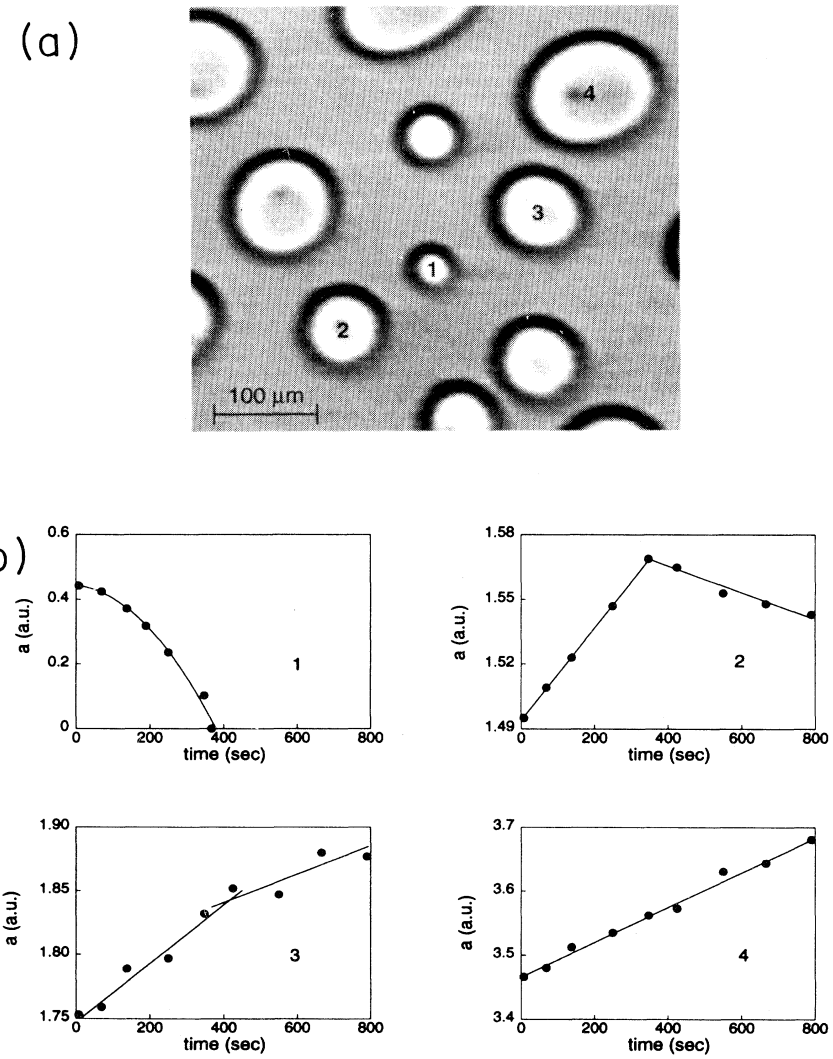

FIG. 8. Evolution of crystals neighboring a shrinking and disappearing crystal: (a) pattern at a given time and (b) the dependence of the areas of crystals as a function of time. Numbers are keyed to part (a). The area fraction is 0.3. The picture was taken 1 h after the run started.

the distribution for $\phi=1.0$ coincides within our experimental uncertainty with the area distribution of froths [36], despite the fact that the line tension of the grain boundaries varies from boundary to boundary.

A glance at the central part of Fig. 2 reveals that the positions of droplets are not random. Spatial correlations are manifested by the tendency of crystals to keep away from each other. This is perhaps more evident when we calculate from these patterns the radial pair distribution function $g(r)$, which is proportional to the probability density of finding two crystals separated by a distance r. This function is shown in Fig. 6 for $\phi=0.13$ and 0.40, with all distances normalized by $\bar{R}$. In measuring $g(r)$ in each case, ten patterns well separated in time were averaged. The broad peak observed for $\phi=0.13$ gives a rough indication of the shell of nearest-neighbor crystals. For $\phi=0.40$ this peak becomes considerably more pronounced, and hence the shell of nearest neighbors becomes more well defined. This signature is reminiscent of the structure induced by repulsive interactions in ordinary fluids, in contrast to the gaslike behavior observed for $\phi=0.13$.

Evidence for the direct correlation effect was obtained by dividing all crystals into two classes, L and S: those with $R>\bar{R}$ (henceforth called *large)* and those with $R<\bar{R}$ (henceforth called *small*), respectively. We then measured the probability densities $p_{s,s'}(r)$ of finding two crystals in the same class ($s=s'=L$ or S) at a distance r, and of finding them in different classes ($s=L$, $s'=S$ or $s=S$, $s'=L$). We plot these with empty and full circles, respectively, in Fig. 7 for both $\phi=0.13$ and $\phi=0.40$. Both probability densities have the same qualitative behavior for $\phi=0.13$, though the probability of finding small crystals near large ones is slightly higher. The correlation is manifestly stronger for $\phi=0.40$, where the probability of finding small crystals near large ones is strongly peaked at small distances and much larger than that of finding two nearby small or large crystals.

In order to exhibit explicitly the medium polarization effect and show the finite range of correlations, we follow the effects of a shrinking crystal upon the evolution of its neighbors. In Fig. 8(a) we show a pattern of crystals observed in one of our runs and in Fig. 8(b) we plot the area of some of them as a function of time [numbers are keyed to Fig. 8(a)]. Crystal number 1 is shrinking monotonously until it disappears. As it shrinks, crystal number 2 grows, but starts shrinking once crystal number 1 disappears. This clearly demonstrates that the concept of critical radius is ill defined for sufficiently large values of ϕ: its value is a function of the local environment of the crystal. Evidence of the finite range of correlations is furnished by the evolution of other neighbors of crystal number 1 while and after the latter shrinks. The rate of growth of crystal number 3 is affected by the shrinkage of crystal number 1. However, the evolution of crystal number 4 is rather insensitive to whatever happens to crystal number 1. If there is indeed an effect, it is buried within the statistical error of our measurements. More quantitatively, we observe medium polarization by studying the spatial distribution of charges. To this end, we define two-point charge-charge spatial correlation functions $g_{qq'}(r)=\langle q(0)q'(r)\rangle$, with q' given in units of charge per unit area. The instantaneous charge of each crystal was deduced from the rate of change of its area, as obtained from video frames taken at close intervals. Five to ten correlation functions calculated at different stages of evolution in the scaling regime were then averaged for each volume fraction. To carry this out, the different correlation functions were rescaled to the same temporal and spatial scales by normalizing all distances by $\bar{R}$ and charges by the condition $\langle q^2\rangle=1$. In order to cope with the calculation of $g_{qq'}(r)$ in our large volume fraction experiments, the charge of each crystal was assumed to be uniformly distributed along its boundary. The total charge within shells of radius r and width Δr around each crystal was then calculated, including only the parts of the boundaries within the shell of all crystals intersected by the shell. Two correlation functions $g_{qq'}(r)$, one with $\mathrm{sgn}(q)=\mathrm{sgn}(q')$ and the other with $\mathrm{sgn}(q)\neq\mathrm{sgn}(q')$, were then calculated. In Fig. 9 we show $g_{qq'}(r)$ for charges of the same sign (empty circles) and charges of opposite sign (full circles), for $\phi=0.13$ and 0.40. The correlation is much larger for short distances in the case of opposite

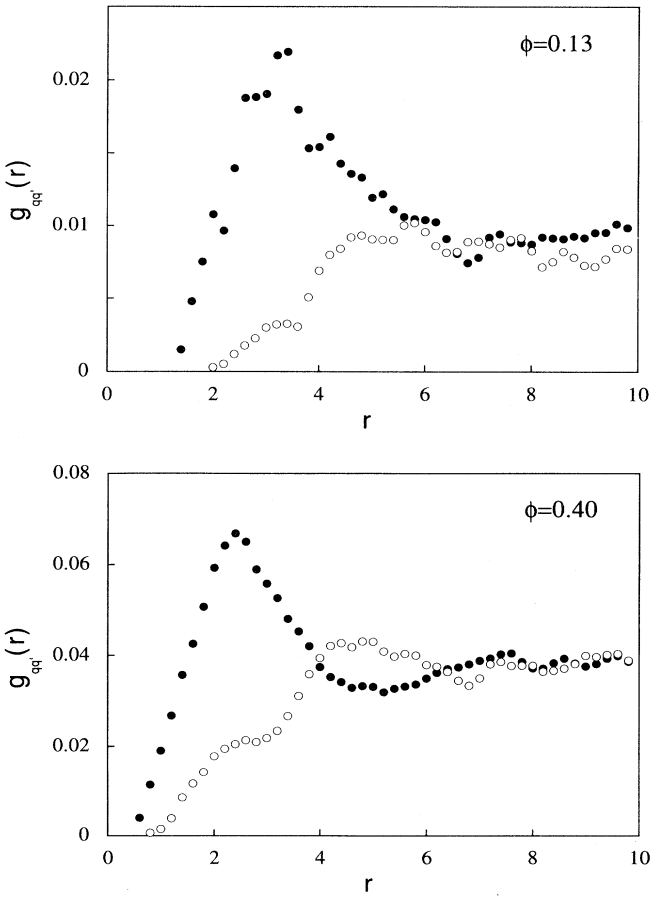

FIG. 9. Radial charge-charge correlation $g_{qq'}(r)$ as function of distance for $\phi=0.13$ and 0.40. Full circles, correlations of charges of opposite sign; empty circles, correlations of charges of the same sign.

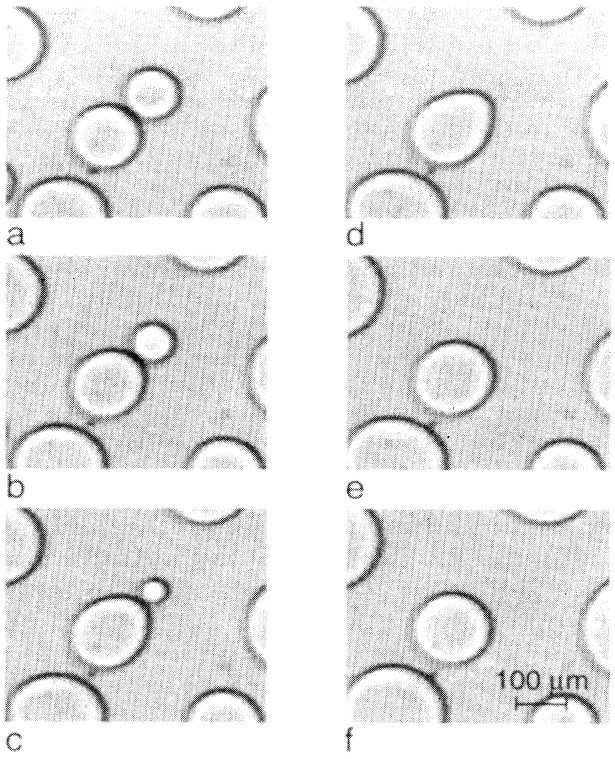

FIG. 10. Snapshots of two nearby crystals, one growing and one shrinking at $\phi=0.30$. Snapshot times: (a) 267, (b) 348, (c) 384, (d) 393, (e) 469, and (f) 575 min after the beginning of the run. Notice the shape distortion of the growing crystal.

charges, and the peak in the correlation corresponds roughly to the average nearest-neighbor distance. Charges of opposite sign screen one another to keep the system locally neutral. The screening effect is much stronger for $\phi=0.40$ where out-of-phase oscillations in both correlations are observed for distances beyond the nearest-neighbor distance, in analogy with behavior observed for ionic liquids.

The direct and medium polarization correlation effects just discussed arise to first order in $\sqrt{\phi}$. In a large-ϕ regime, higher-order effects such as changes in crystal shape and center-of-mass displacements become appreciable. These effects are readily observed in our experiments. In Fig. 10 we follow the evolution of two nearby crystals. As the system evolves the small crystal shrinks while the large one grows more rapidly in the direction of its shrinking neighbor, becoming considerably distorted. Finally, when the small crystal has disappeared the large one relaxes back to a quasicircular shape. Clearly, this behavior cannot be accounted for by a monopole approximation to the diffusion field. Imaeda and Kawasaki have shown using a multipole expansion of the diffusion field

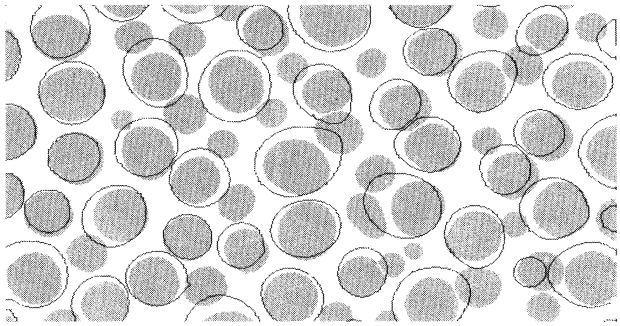

FIG. 11. Migration of the center of mass of crystals during evolution for $\phi=0.54$. The shaded shapes represent a digitized image of a pattern of crystals at an early time during evolution, while the contours represents the surviving crystals at a later time. The pictures were taken 7 and 16 h after the beginning of the run. The image is about 2.5 mm across.

that both effects tend to accelerate the coarsening process [40]. Moreover they showed that the deformation is a manifestation of the Mullins-Sekerka instability and they computed the evolution of droplet shapes droplet deformation in the two-dimensional case. The shapes obtained by Imaeda and Kawasaki look remarkably close to those observed in Fig. 10. Finally, we show in Fig. 11 the superposition of two patterns of crystals, one at an early time during the evolution (shaded shapes), while the other (contours) represents the surviving crystals at a later time. Displacements of the centers of mass are evident in large crystals that have gobbled up small ones. Notice that the displacements are directed towards the position of the shrinking crystals. We have not studied quantitatively the dependence of the average displacement on volume fraction.

In summary, our results show that diffusional interactions in a two-dimensional system undergoing Ostwald ripening at $\phi\neq 0$ give rise to liquidlike spatial structure among the droplets of the minority phase for sufficiently large values of ϕ, and induce correlations between their sizes and rates of growth. The former are weaker than the latter in agreement with recent theoretical models. Structural effects in particular should be taken into account in any future theoretical description of large volume fraction situations. In addition, we have shown that for large enough values of ϕ, interactions give rise to considerable distortions in the droplets' shape as well as to displacement in their centers of mass. We hope our results will stimulate further research into the problem, and provide a useful benchmark to which more refined calculations can be compared.

ACKNOWLEDGMENTS

We are indebted to E. Domany and B. Levitan for useful discussions. This research was supported by the Charles H. Revson and the Minerva Foundations (J.S.).

[1] For a review see J. D. Gunton, M. San Miguel, and P. S. Sahni, in *Phase Transitions and Critical Phenomena,* edited by C. Domb (Academic, New York, 19xx), Vol. 8, and references therein.
[2] W. Ostwald, *Grundriss, der Allgem. Chemie* (Macmillan, London, 1908), p. 96; *Foundations of Analytic Chemistry,* 3rd English ed. (Macmillan, London, 1908), p. 22; *Principles of Inorganic Chemistry* (Macmillan, London, 1902), p. 258.
[3] I. M. Lifshitz and V. V. Slyozov, Zh. Eksp. Teor. Fiz. **35**, 479 (1958) [Sov. Phys. JETP **8**, 331 (1959)]; J. Phys. Chem. Solids **19**, 35 (1961); Sov. Phys. Solid State **1**, 1285 (1960).
[4] C.Wagner,Z. Elektrochem. **65**, 581 (1961).
[5] P. K. Rastogi and A. J. Ardell, Acta. Metall. **19**, 321 (1971).
[6] D. H. Jack and R. W. K. Honeycombe, Acta. Metall. **20**, 787 (1972).
[7] Y.Seno *et al.*, Trans. Jpn. Inst. Met. **24**, 491 (1983).
[8] G. P. Wirtz and M. E. Fine, J. Am. Ceram. Soc. **51**, 402 (1968).
[9] T. Hirata and D. H. Kirkwood, Acta. Metall. **25**, 1425 (1977).
[10] D. J. Chellman and A. J. Ardell, Acta. Metall. **22**, 577 (1974).
[11] S. C. Hardy and P. W. Voorhees, Metall. Trans. A **19**, 2713 (1988).
[12] A. N. Niemi and T. H. Courtney, J. Mater. **29**, 226 (1981).
[13] S. S. Kang and D. N. Yoon, Metall. Trans. A **13**, 1405 (1982).
[14] P. W. Voorhees, G. B. McFadden, R. F. Boisvert, and D. I. Meiron, Acta Metall. **36**, 207 (1988).
[15] N. Akaiwa and P. W. Voorhees, Phys. Rev. E **49**, 3860 (1994).
[16] P. W. Voorhees and M. E. Glocksman, Acta. Metall. **32**, 2001 (1984).
[17] J. H. Yao, K. R. Eldeer, H. Guo, and M. Grant, Phys. Rev. B **45**, 8173 (1992); Physica (Amsterdam) **204A**, 770 (1994).
[18] P. W. Voorhees and R. J. Schaefer, Acta Metall. **35**, 327 (1987).
[19] J. J. Weins and J. W. Cahn, in *Sintering and Related Phenomena,* edited by G. C. Kuczynski (Plenum, London, 1973), p. 151.
[20] J. A. Marqusee and J. Ross, J. Chem. Phys. **80**, 536 (1984).
[21] M. Tokuyama and K. Kawasaki, Physica (Amsterdam) **123A**, 386 (1984).
[22] M. Marder, Phys. Rev. Lett. **55**, 2953 (1985); Phys. Rev. A **36**, 858 (1987).
[23] T. M. Rogers and R. C. Desai, Phys. Rev. B **39**, 11 956 (1989).
[24] B. K. Chakraverty, J. Phys. Chem. Solids **28**, 2401 (1967).
[25] D. B. Dadyburjor, S. P. Marsh, and M. E. Glicksman, J. Catal. **99**, 358 (1986).
[26] H. Hayakawa and F. Family, Physica (Amsterdam) **163A**, 491 (1990).
[27] A. J. Ardell, Acta. Metall. **20**, 61 (1972); Phys. Rev. B **41**, 2554 (1990).
[28] J. A. Marqusee, J. Chem. Phys. **81**, 976 (1984).
[29] Q. Zheng and J. D. Gunton, Phys. Rev. A **39**, 4848 (1989).
[30] A. Chakrabarti, R. Toral, and J. D. Gunton, Phys. Rev. E **47**, 3025 (1993).
[31] P. Bassereau, D. Brodbreck, T. P. Russel, H. R. Brown, and K. R. Shull, Phys. Rev. Lett. **71**, 1716 (1993).
[32] M. Seul, N. Y. Morgan, and C. Sire (to be published).
[33] H. Tanaka, T. Yokokawa, H. Abe, T. Hayashi, and T. Nishi, Phys. Rev. Lett. **65**, 3136 (1990).
[34] O. Krichevsky and J. Stavans, Phys. Rev. Lett. **70**, 1473 (1993).
[35] K. Kawasaki and T. Ohta, Physica (Amsterdam) **118A**, 175 (1983).
[36] J. Stavans, Rep. Prog. Phys. **56**, 733 (1993).
[37] J. Von Neumann, *Metal Interfaces* (American Society for Metals, Cleveland, 1952), p. 108.
[38] V. E.Fradkov, M. E. Glicksman, M. Palmer, J. Nordberg, and K. Rajan, Physica (Amsterdam) **66D**, 50 (1993).
[39] B. Levitan and E. Domany (to be published).
[40] T. Imaeda and K. Kawasaki, Physica (Amsterdam) **164A**, 335 (1990).

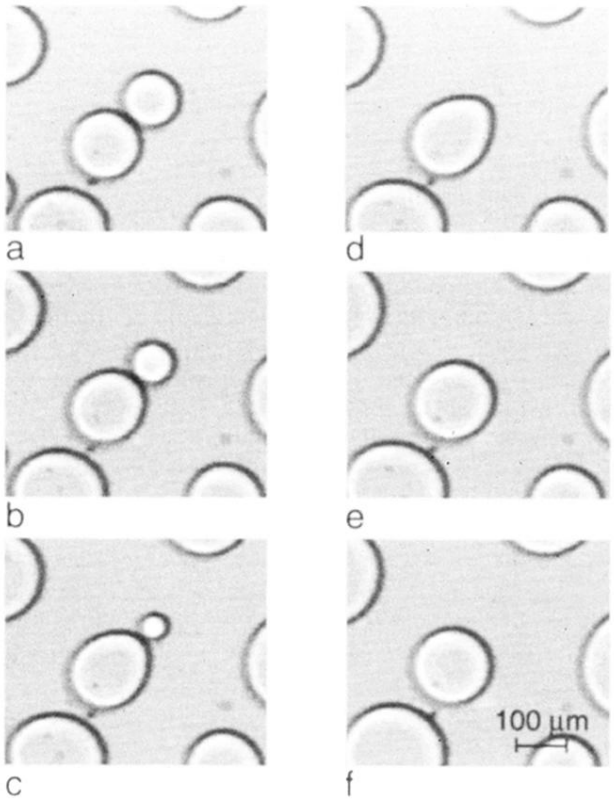

FIG. 10. Snapshots of two nearby crystals, one growing and one shrinking at $\phi=0.30$. Snapshot times: (a) 267, (b) 348, (c) 384, (d) 393, (e) 469, and (f) 575 min after the beginning of the run. Notice the shape distortion of the growing crystal.

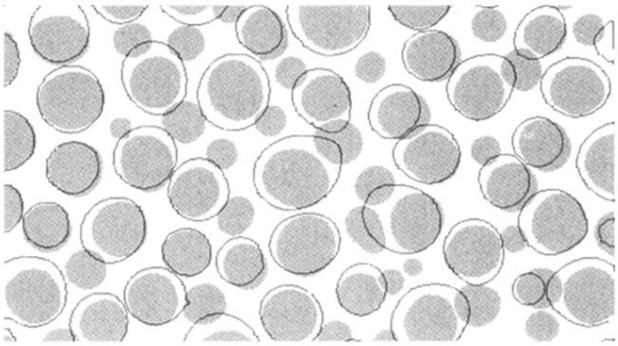

FIG. 11. Migration of the center of mass of crystals during evolution for $\phi=0.54$. The shaded shapes represent a digitized image of a pattern of crystals at an early time during evolution, while the contours represents the surviving crystals at a later time. The pictures were taken 7 and 16 h after the beginning of the run. The image is about 2.5 mm across.

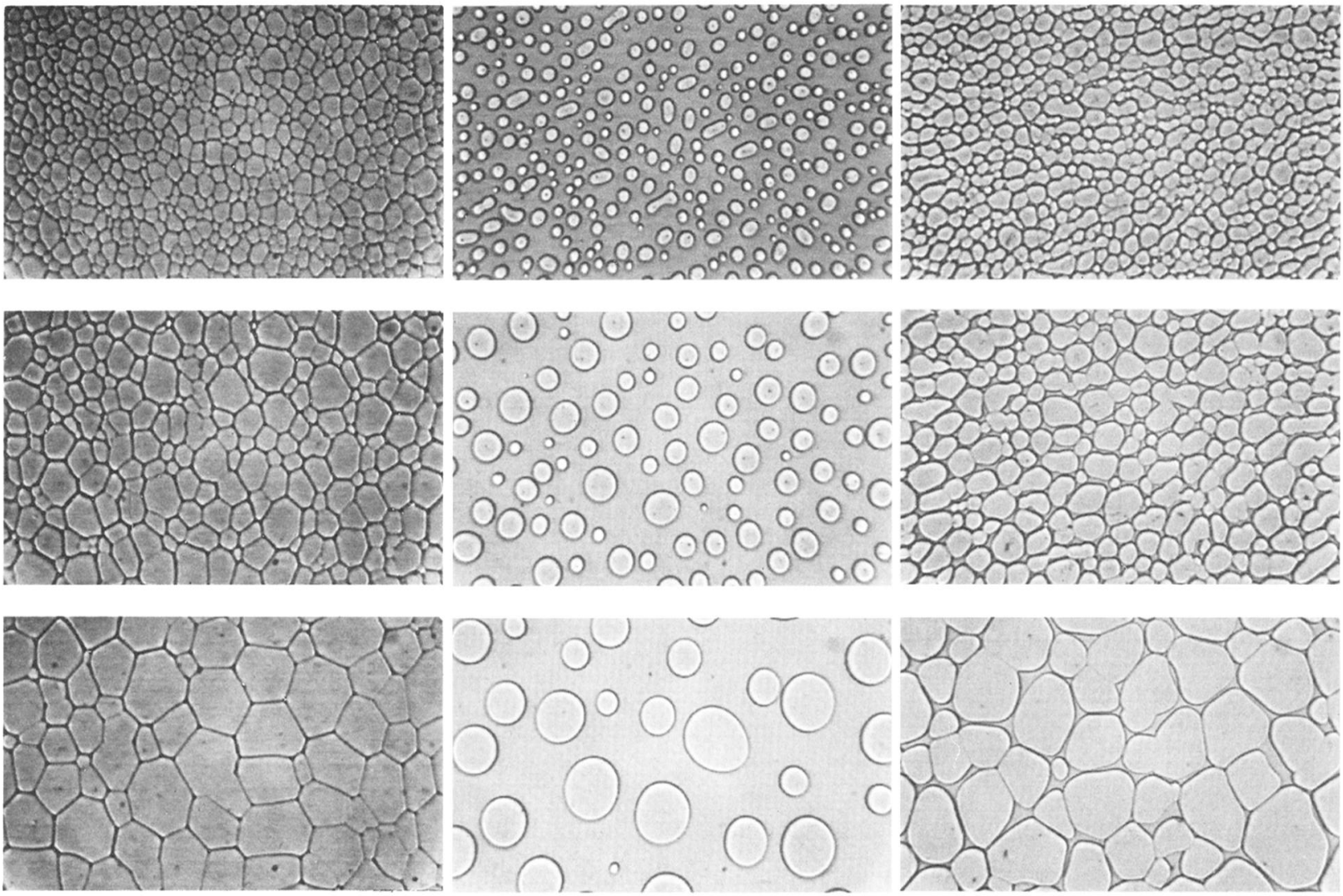

FIG. 2. Snapshots of part of the system coarsening at three different values of the temperature T. Left: cellular structure evolution ($\phi=1$) at $T=38\,^{\circ}\mathrm{C}$ (snapshot times from top to bottom: 15, 110, and 540 min); center: coarsening at $T=54\,^{\circ}\mathrm{C}$ where crystals are well separated, filling a fraction $\phi=0.3$ of the total area (times: 16, 145, and 1440 min); right: partial melting along grain boundaries at $T=43\,^{\circ}\mathrm{C}$ (times: 20, 120, and 1440 min). The images are about 2.5 mm across.

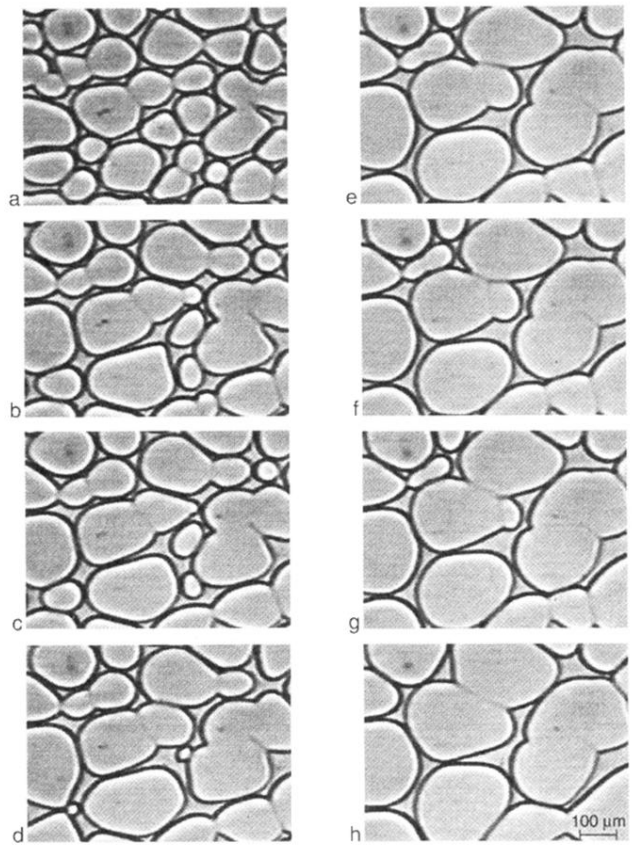

FIG. 3. Evolution of a region in our system at $T = 43\,^{\circ}\mathrm{C}$. Snapshot times: (a) 104, (b) 260, (c) 291, (d) 342, (e) 505, (f) 536, (g) 563, and (h) 679 min. Focusing on the central part of each snapshot, notice the presence of two evolution processes: the Ostwald ripening mechanism (a) and (b), and recrystallization events such as creation (c)–(f), and disappearance (g) and (h) of grain boundaries. The area fraction is 0.9 in this case.

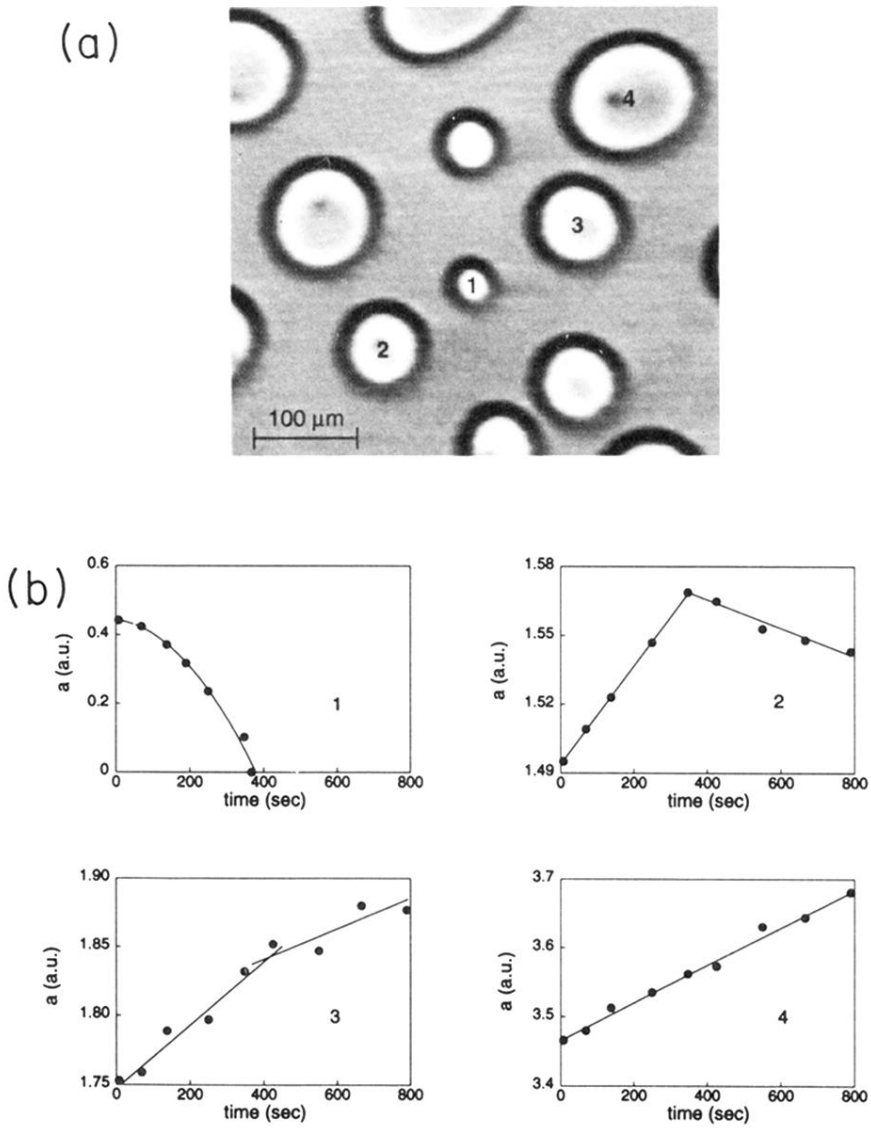

FIG. 8. Evolution of crystals neighboring a shrinking and disappearing crystal: (a) pattern at a given time and (b) the dependence of the areas of crystals as a function of time. Numbers are keyed to part (a). The area fraction is 0.3. The picture was taken 1 h after the run started.